Effect of a thin weak layer at around the 660-km discontinuity on subducting slab morphology in the mantle transition zone

Zhong-Hai Li[1] and Ling Chen[2]

[1]University of Chinese Academy of Sciences
[2]Institute of Geology and Geophysics, Chinese Academy of Sciences

November 24, 2022

Abstract

The subducting slab morphology in the mantle transition zone (MTZ) is strongly affected by the mantle viscosity and density variations at the 660-km discontinuity (D660). Besides the negative Clapeyron slope of phase transition and the viscosity increase, a possible thin weak layer at around D660 is proposed to play a key role in the slab stagnation, which is however not well constrained. In this study, a series of numerical models are systematically conducted, which reveal that a weak layer beneath D660 does not change the slab mode selection (penetration versus stagnation). However, it will contribute to longer slab flattening at the bottom of the MTZ, when slab sinking is strongly resisted by either the viscosity increase or a large Clapeyron slope at D660. The role of a weak layer on slab flattening is dependent on the lubrication effect that promotes sub-horizontal slab movement at the bottom of the MTZ.

Effect of a thin weak layer at around the 660-km discontinuity on subducting slab morphology in the mantle transition zone

Zhong-Hai Li [1], Ling Chen [2,3]

[1] Key Laboratory of Computational Geodynamics, College of Earth and Planetary Sciences, University of Chinese Academy of Sciences, Beijing, China

[2] State Key Laboratory of Lithospheric Evolution, Institute of Geology and Geophysics, Chinese Academy of Sciences, Beijing, China

[3] CAS Center for Excellence in Tibetan Plateau Earth Sciences, Beijing, China

Highlights:

(1) A weak layer above 660-km discontinuity, at 610-660 km, has negligible effect on the slab morphology in the mantle transition zone (MTZ).

(2) A weak layer beneath 660-km discontinuity, at 660-710 km, does not change the slab mode selection (penetration versus stagnation).

(3) A weak layer at 660-710 km contributes to sub-horizontal slab movement and flattening in MTZ in case with high resistance from lower mantle.

Abstract:

The subducting slab morphology in the mantle transition zone (MTZ) is strongly affected by the mantle viscosity and density variations at the 660-km discontinuity (D660). Besides the negative Clapeyron slope of phase transition and the viscosity increase, a possible thin weak layer at around D660 is proposed to play a key role in the slab stagnation, which is however not well constrained. In this study, a series of numerical models are systematically conducted, which reveal that a weak layer beneath D660 does not change the slab mode selection (penetration versus stagnation). However, it will contribute to longer slab flattening at the bottom of the MTZ, when slab sinking is strongly resisted by either the viscosity increase or a large Clapeyron slope at D660. The role of a weak layer on slab flattening is dependent on the lubrication effect that promotes sub-horizontal slab movement at the bottom of the MTZ.

Plain Language Summary

On the Earth, an oceanic plate may sink down beneath another plate into the subjacent mantle, which is called ‘subduction’. The mantle is not homogeneous, but generally divided into the upper and lower mantle with different mineral phases. The boundary locates at about 660 km depth, which is characterized by the downward density and viscosity increase, as well as the possible existence of a thin weak layer. Thus the sinking slab could be strongly affected by the 660-km discontinuity (D660), resulting in variable slab morphologies as revealed by geophysical observations. A key point is about the effect of the thin weak layer on the mode selection of sinking slab. A previous modeling study proposed that the weak layer has a critical effect on slab stagnation above D660, rather than penetrating into the lower mantle. However, the current systematic models reveal that a weak layer beneath D660 does not change the slab mode selection (penetration versus stagnation), although it will contribute to sub-horizontal slab movement and longer-distance flattening at the bottom of the MTZ in case with high resistance from the lower mantle.

1. Introduction

The morphology and dynamics of subducting slabs are strongly controlled by the rheological structure and layering of the Earth's mantle (e.g., *Gurnis & Hager, 1988; Čížková et al., 2002; Billen, 2010; Agrusta et al., 2017; Goes et al., 2017; Yang et al., 2018; Li et al., 2019*), which are however not well understood. The radial viscosity profile is generally inferred from the joint inversions of glacial isostasy adjustment data, geoid anomalies, as well as constraints from mineral physics (*Hager et al., 1985; Forte and Peltier, 1987, 1991; Ricard and Bai, 1991; King and Masters, 1992; Ricard et al., 1993; Corrieu et al., 1995; Forte and Mitrovica, 1996; Lambeck et al., 1996, 1998; Mitrovica and Forte, 2004; Steinberger and Calderwood, 2006; Forte et al., 2010*), which shows that the average viscosity of the lower mantle is 10-100 times higher than the average upper mantle viscosity (Figure S1 in the supporting information) (*Zhu, 2016*). However, it is widely debated about the rheological transition mode between the upper and lower mantle, for example, a sharp viscosity jump or a gradual viscosity increase (Figure S1).

Besides the rheological contrast, the phase transition at the 660-km discontinuity (D660), i.e., the bottom of the mantle transition zone (MTZ) in between the upper and lower mantle, is characterized by a negative Clapeyron slope of $C_{660} \in [-4.0, -0.4]$ MPa/K according to a number of high-pressure laboratory experiments as summarized in *Li et al.* (2019). Many modeling studies have been conducted to investigate how a slab interacts with D660, and generally suggest that a higher Clapeyron slope contributes significantly to the stagnation of subducting slab in the MTZ (*Goes et al., 2017; Li et al., 2019;* and references therein).

Another key point is about a thin weak layer at around the bottom of the MTZ proposed in some of the joint inversion models (e.g., *Mitrovica and Forte, 2004*; Figure S1). The formation mechanism of this possible weak layer is still not clear, which may be caused by grain size reduction and/or superplasticity (*Karato, 2008*), the presence of water (*Tschauner et al., 2018*), or a partially molten carbonated layer (*Sun et al., 2018*). Geodynamic models have shown that a weak layer beneath D660 may have a large effect on either mantle plume branching (*Liu and Leng, 2020*) or subducting slab stagnation (*Mao and Zhong, 2018*).

The upper/lower mantle boundary, i.e. D660 characterized by strong density and viscosity variations, is thus a critical structure for mantle dynamics. The general effects of the Clapeyron slope (C_{660}) and viscosity jump on the morphology of subducting slabs have been widely modeled and investigated; however, the influence of a possible weak layer at around this discontinuity lacks systematic studies. *Mao and Zhong* (2018) proposed that this weak layer plays significant roles in the slab flattening in the MTZ, by conducting a 3-D global model and further comparing their results with seismic tomographic images. However, it remains difficult to isolate the effect of the weak layer in the complex model with prescribed surface velocities and trench motions, as well as the interactions among global subduction zones. Thus, the exact role of this weak layer, as well as the mechanism of its control on slab stagnation, is still not clear. In this study, we aim to solve this problem by applying a more generic, pure dynamic subduction model, focusing on the effects of density and viscosity variations across the weak layer at around D660.

2. Initial model setup

Numerical models are conducted with the code I2VIS (*Gerya, 2010*), which is integrated with the deep water activity and phase transitions down to 30 GPa in the deep mantle. The detailed numerical methods and implementations are shown in *Li et al.* (2019) and the supporting information (Text S1).

Large-scale numerical models are set up in a Cartesian box of 5000 × 1400 km (Figure 1). In the initial model, an oceanic plate is set on the left and a continental plate on the right, with an initial weak zone in between (Figure 1a). The oceanic lithosphere includes an upper- (3 km) and a lower-crustal layer (5 km), as well as a mantle layer with the thickness dependent on the lithospheric age (60 Ma). The initial thermal structure of the oceanic lithosphere is defined by the half-space cooling model (*Turcotte and Schubert, 2002*). The continental lithosphere includes an upper crust (20 km), a lower crust (15 km) and a mantle layer (100 km), with the initial thermal structure defined by a linear gradient from 0°C at the surface to 1350°C at the bottom.

The initial thermal gradient in the sub-lithospheric mantle is defined by a constant value of 0.5 °C/km. On the top of the model domain, a ‘sticky air’ layer with low density and viscosity is applied (*Schmeling et al., 2008; Crameri et al., 2012*). Detailed numerical parameters are shown in Tables S1 and S2 in the supporting information.

For the effective viscosity of multiple rock types, the composite visco-plastic-Peierls rheology is generally applied (Text S1 and Table S1). It results in a rheologically strong lithosphere and a weak asthenospheric layer beneath (Figure 1d-e). Then the effective viscosity increases downward to the MTZ and lower mantle, which is generally consistent with the viscosity profiles inferred from the more recent joint observations (red and blue lines in Figure 1e) (*Mitrovica and Forte, 2004; Forte et al., 2010*). The effect of the weak layer at the bottom of the MTZ (Figure 1e; *Mitrovica and Forte, 2004*) or beneath the MTZ as in *Mao and Zhong* (2018) is the focus of this study and thus systematically investigated. In addition, the effect of an abrupt viscosity jump at D660 is further tested, by applying various constant viscosities in the lower mantle (Figure 1e).

For the boundary conditions of the model, free slip is satisfied for all boundaries. In addition, a constant convergence velocity of 5 cm/yr (Vsp = 4 cm/yr, Vop = -1 cm/yr; Figure 1a) is applied for subduction initiation, which will be canceled after 10 Myrs. For the thermal boundary conditions, fixed values of 0ºC and 1975ºC are applied for the top and bottom boundaries, respectively. The vertical boundaries have no horizontal heat flux.

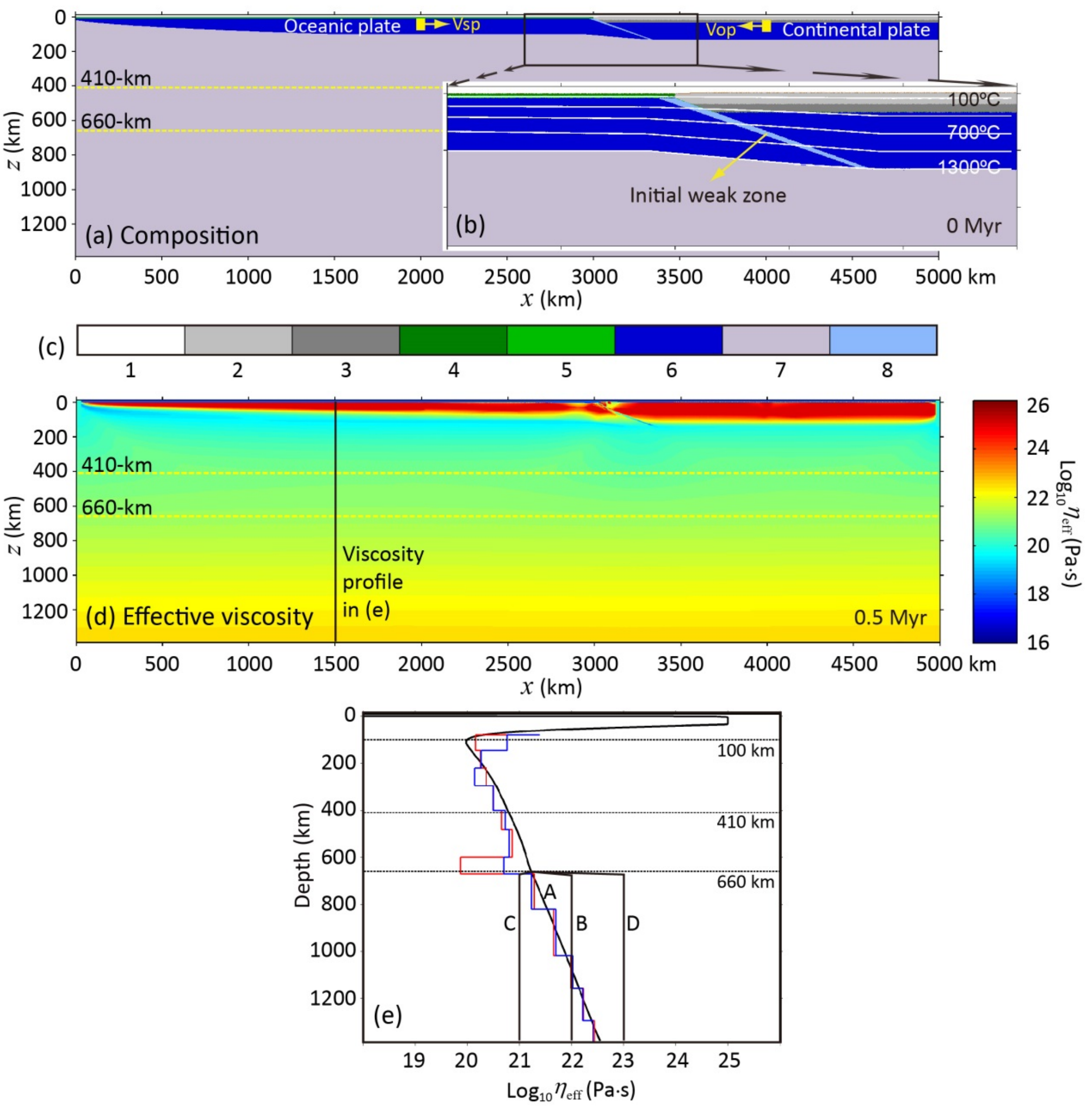

Figure 1. Initial model configuration. (a) Composition field in the framework of 5000 × 1400 km, with the 410-km and 660-km discontinuities shown with yellow dashed lines (phase transitions illustrated in Text S1 of the supporting information). (b) The enlargement of initial subduction zone, with white lines for isotherms, starting from 100°C with the interval of 300°C. The colors in (a) and (b) indicate for rock types as specified in (c): 1-sticky air; 2,3-continental upper and lower crust, respectively; 4,5-oceanic upper and lower crust, respectively; 6,7-lithospheric and subjacent mantle, respectively; 8-hydrated mantle. It is worth noting that the additional rock types, e.g., the partially molten rocks, are not shown in the initial model, but will appear during the evolution of the model. (d) The effective viscosity field of the model, with a vertical profile as the A-Type shown in (e). The composite rheology is applied for A-type (Text S1 in the supporting information), with effective viscosity increasing

downward in the lower mantle, which is generally consistent with the viscosity profiles inferred from the joint observations (red and blue lines) (*Mitrovica and Forte, 2004; Forte et al., 2010*). Three additional types of numerical models are conducted with different, but constant viscosities of the lower mantle, i.e. 10^{22} Pa·s (B), 10^{21} Pa·s (C) and 10^{23} Pa·s (D), respectively.

3. Model results

3.1. Reference models with composite rheology of the lower mantle

In this section, the composite rheology is applied for all the rock types, with an effective viscosity profile (A-type) shown in Figure 1e. The effect of a weak layer is systematically studied, which is 50 km thick and has a constant viscosity of 10^{20} Pa·s. The weak layer is positioned either above or beneath D660 (Figure 2), the results of which are further compared with the model without such a weak layer. In addition, the sensitivity tests with variable Clapeyron slopes at D660 are conducted.

The modeling and comparison results demonstrate that the existence of such a weak layer does not change the general slab mode selection between penetration and stagnation (Figure 2). In the models with a large Clapeyron slope of C_{660} = -4 MPa/K, a weak layer beneath D660 can increase the length of the stagnant slab in the MTZ, comparing to the models without the weak layer or with it above D660 (c.f. Figures 2e, 2j, 2o). It indicates that the weak layer beneath D660 promotes the sub-horizontal movement of the stagnant slab at the bottom of the MTZ, facilitated by the large resistance to the sinking slab due to the large negative Clapeyron slope and the resulting delay of phase transition.

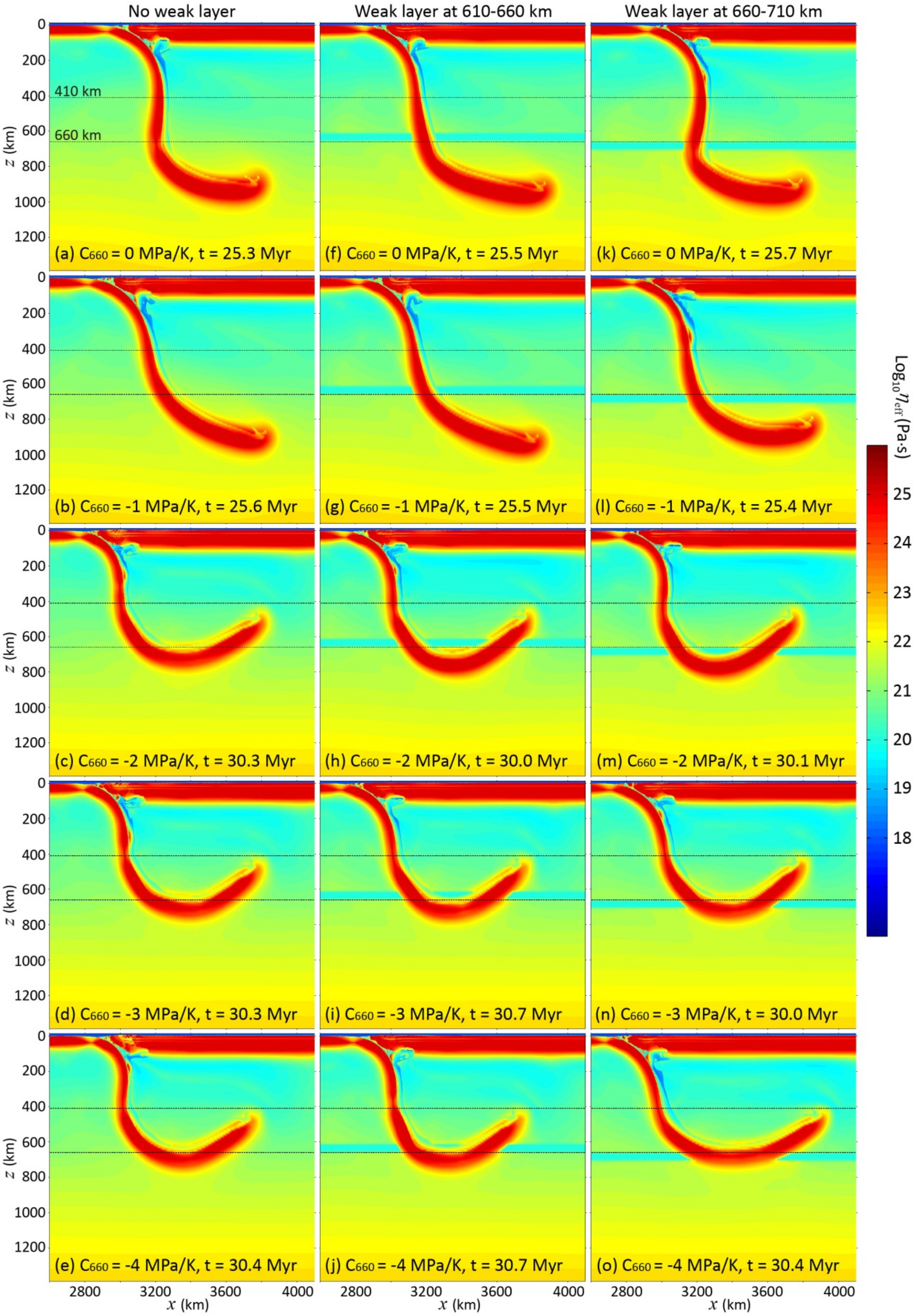

Figure 2. Model results with a composite rheological profile of the lower mantle, i.e. A-type in Figure 1e. The effects of a thin weak layer and the Clapeyron slope (C_{660}) at D660 are tested.

3.2. Models with intermediate and constant viscosity of the lower mantle (10^{22} Pa·s)

In this set of models, a constant viscosity of 10^{22} Pa·s is applied for the lower mantle, with an effective viscosity profile shown in Figure 1e (B-type), which is more or less the average value of the A-type gradually increasing viscosity in the lower mantle.

The model results are quite similar to the ones with composite rheology of the lower mantle (c.f. Figures 3 and 2), which indicate that a sharp viscosity jump has a similar dynamic effect as an equivalent, strong viscosity-depth gradient between the lower and upper mantle. The influence of the weak layer is only obvious in the models with a high Clapeyron slope of C_{660} = -4 MPa/K, which indicates again that a weak layer beneath D660 may lead to longer slab stagnation in the MTZ (c.f. Figures 3e, 3j, 3o), similar to the reference models in Figure 2.

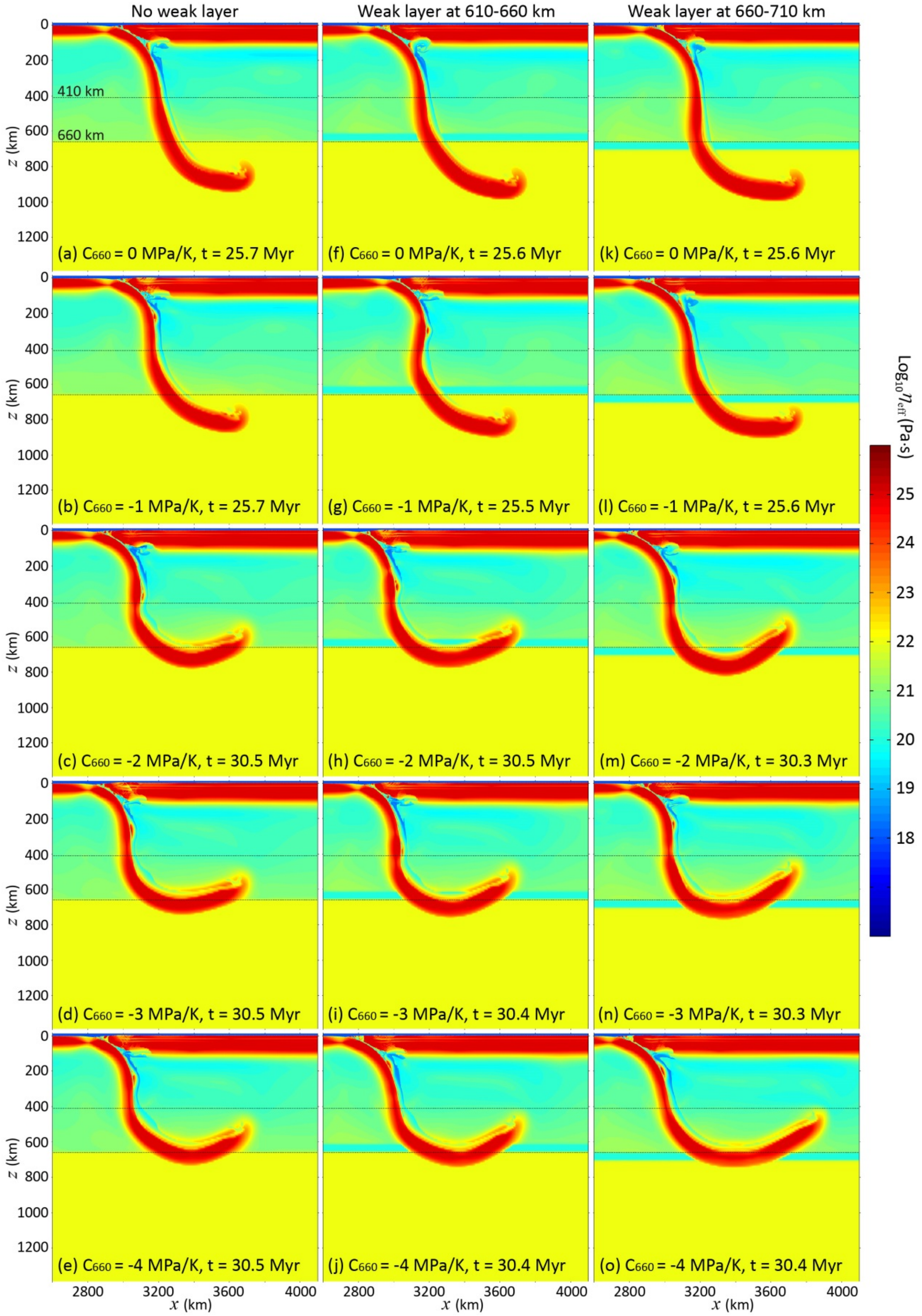

Figure 3. Model results with a constant viscosity (10^{22} Pa·s) of the lower mantle, i.e. B-type in Figure 1e. The effects of a thin weak layer and the Clapeyron slope (C_{660}) at D660 are tested.

3.3. Models with low and constant viscosity of the lower mantle (10^{21} Pa·s)

In this set of models, a constant viscosity of 10^{21} Pa·s is applied for the lower mantle, with an effective viscosity profile shown in Figure 1e (C-type), which represents an end-member regime with the rheologically weakest lower mantle.

The model results show that the sinking slab can easily penetrate the MTZ to the lower mantle, with the Clapeyron slope of $|C660| \leq 3$ MPa/K (Figure 4). It indicates that the weak lower mantle does not provide enough resistance for the slab stagnation. In contrast, with a large Clapeyron slope of $C_{660} = -4$ MPa/K, the slab stagnates and flattens at the bottom of the MTZ, mainly due to the delay of phase transition and the consequent low density of sinking slab compared to the neighboring lower mantle, which thus provides large resistance on the subducting slab. In this set of models, the weak layer, no matter above or beneath D660, does not affect the slab morphology in the MTZ (Figure 4).

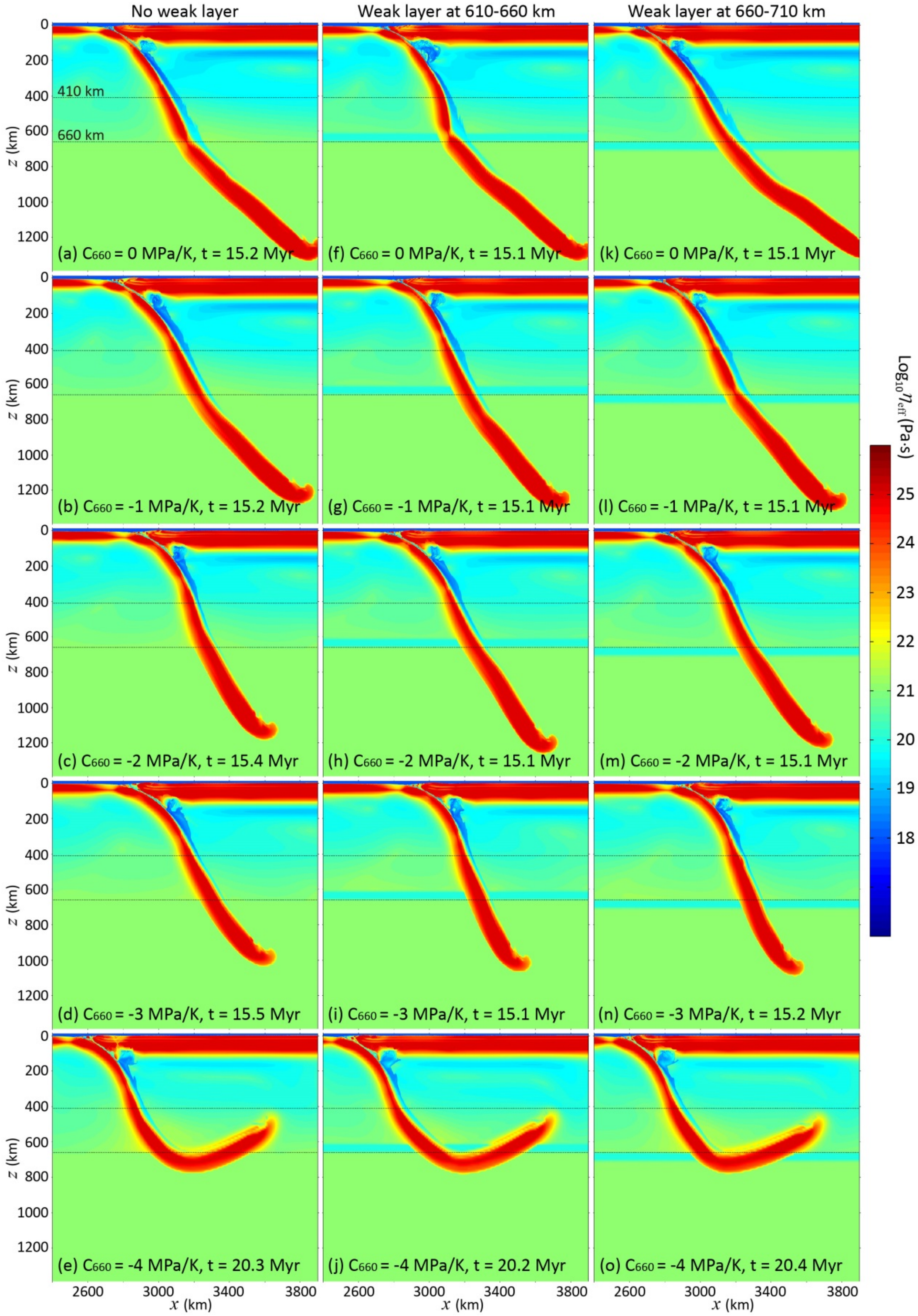

Figure 4. Model results with a constant viscosity (10^{21} Pa·s) of the lower mantle, i.e. C-type in Figure 1e. The effects of a thin weak layer and the Clapeyron slope (C_{660}) at D660 are tested.

3.4. Models with high and constant viscosity of the lower mantle (10^{23} Pa·s)

In this set of models, a constant viscosity of 10^{23} Pa·s is applied for the lower mantle, with an effective viscosity profile shown in Figure 1e (D-type), which represents an end-member regime with the rheologically strongest lower mantle.

In all the models, the slab stagnation is predicted due to the strong resistance from the lower mantle (Figure 5); however, the lengths of the flattened slab are different at the bottom of the MTZ. It shows that the weak layer above D660, i.e. at 610-660 km, does not affect the morphology of the stagnant slab in the MTZ (c.f. first and second columns of Figure 5). In contrast, the weak layer beneath D660, i.e. at 660-710 km, contributes significantly to the long slab flattening in the MTZ, which can be further promoted by a larger Clapeyron slope (C_{660}). It indicates that the weak layer beneath D660 facilitates the sub-horizontal movement of the flat slab at the bottom of the MTZ, in cases with large resistance from the lower mantle to slab sinking.

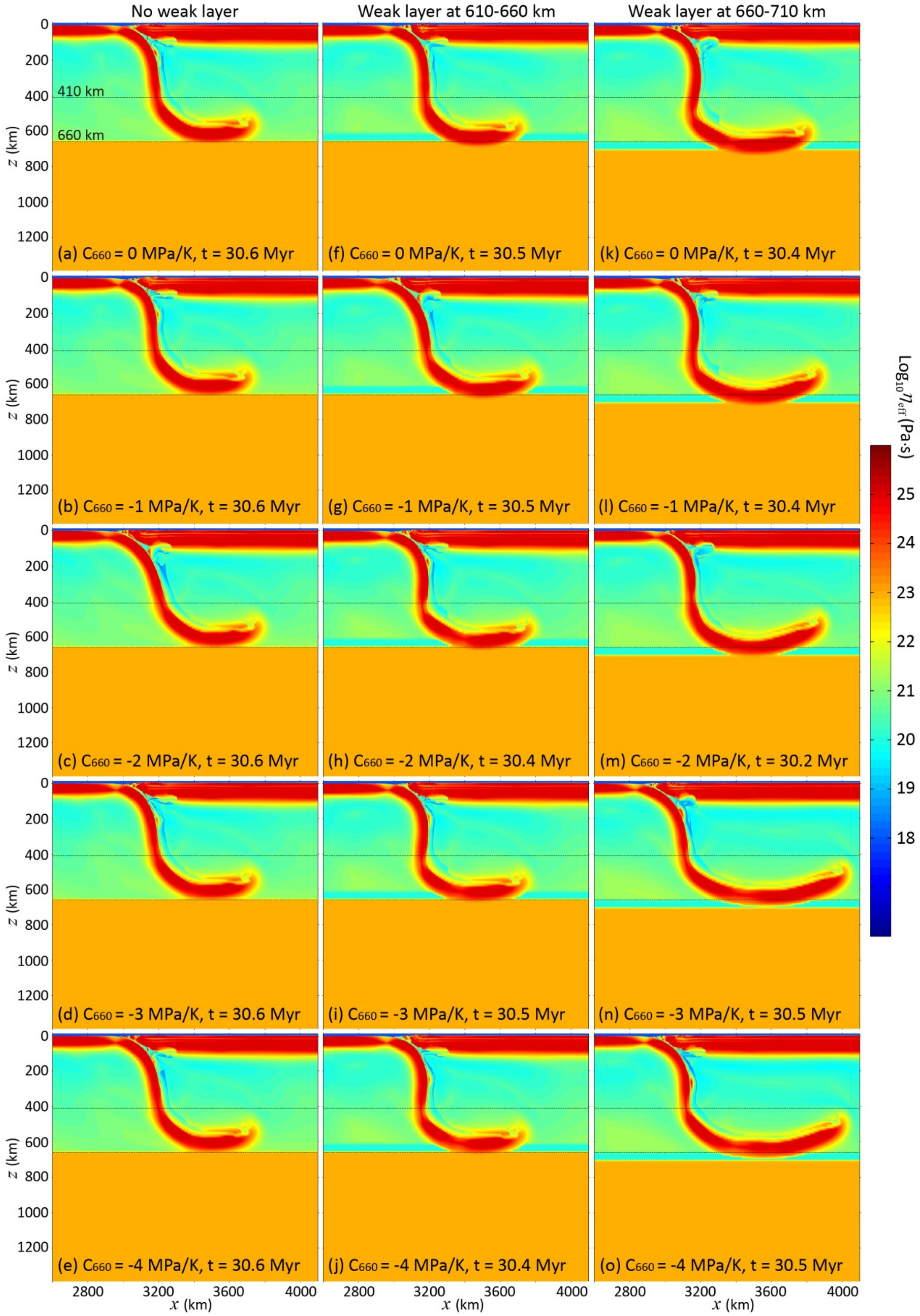

Figure 5. Model results with a constant viscosity (10^{23} Pa·s) of the lower mantle, i.e. D-type in Figure 1e. The effects of a thin weak layer and the Clapeyron slope (C_{660}) at D660 are tested.

4. Discussion

4.1. The role of a weak layer between the upper and lower mantle on slab dynamics

The systematic numerical models indicate that a thin weak layer above D660, i.e. at 610-660 km depth, has negligible effects on the subducting slab morphology in all the cases (Figures 2-5). Alternatively, if the weak layer is set at 660-710 km depth, it still does not change the general slab mode selection (penetration versus stagnation) in the MTZ. However, when the strong resistance of the lower mantle is acting on the sinking slab, the weak layer contributes to longer slab flattening at the bottom of the MTZ. The resistance could result from either a large Clapeyron slope of phase transition at D660 (e.g., Figures 2o and 3o) or a sufficient increase in the viscosity of the lower mantle (Figures 5k-n), or both (Figure 5o).

Figure 6 shows detailed analyses of the effects of a thin weak layer on the slab dynamics. In the regime with a weak layer at 610-660 km depth, the subducting slab sinks down, reaches the weak layer and finally touches the lower mantle (Figure 6b). Then the direct contact between the rheologically strong slab and lower mantle hinders the sub-horizontal movement of the slab along the weak layer at the bottom of the MTZ, which thus results in a similar slab mode as that without such a weak layer (Figure 6a). In an alternative regime with a weak layer at 660-710 km depth, the subducting slab arrives at D660 first. The lower density of the slab, due to the negative C_{660} and delayed phase transition, leads to slab 'floating' above/into the weak layer (Figures 6c, 6c'). In this case, the presence of a 'lubrication' layer between the rheologically strong slab and lower mantle, combining with the decreased negative buoyancy of the slab, can significantly reduce the shear resistance during the sub-horizontal slab movement (Figure 6e). It thus leads to a longer slab flattening at the bottom of the MTZ (e.g., the third column in Figure 5).

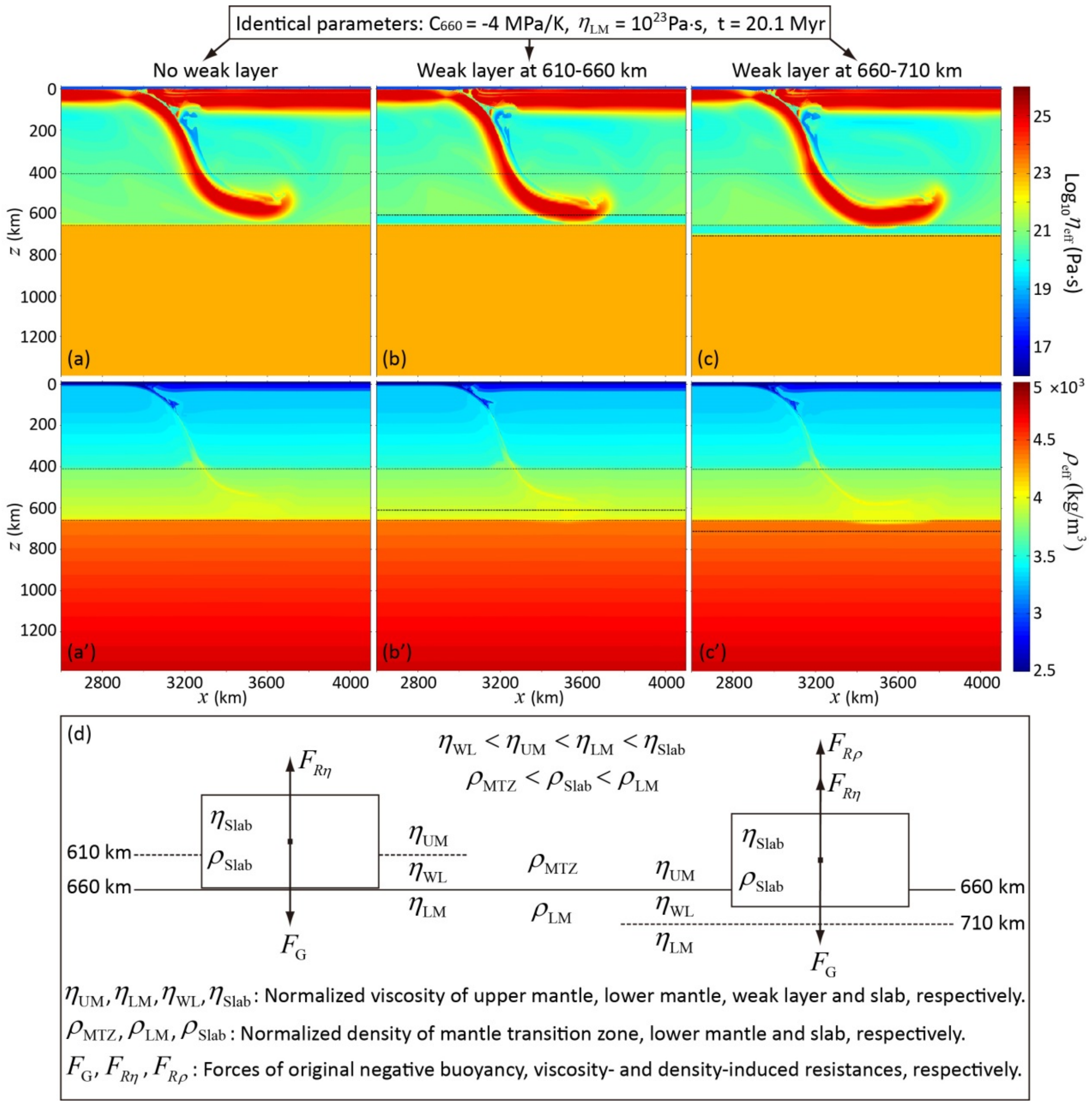

Figure 6. Comparison and analysis of the effects of a thin weak layer at around D660. (a-c) The effective viscosity fields of the end-member models with the highest lower mantle viscosity (10^{23} Pa·s) and largest Clapeyron slope of C_{660} = -4 MPa/K, which are the same as those in Figures 5e, 5j and 5o, respectively, but at an earlier time of 20.1 Myr. (a'-c') The corresponding density fields of the three models (a-c), respectively. (d) The force balance analyses of a simple stagnant slab in the MTZ, with a weak layer at 610-660 km (left) or 660-710 km (right).

It is worth noting that the slab 'skating' along the weak layer may only exist for a certain time from the initial interaction of the slab with D660. Finally, the slab may sink and touch the rheologically strong lower mantle as shown in Figures 2-5, with the timespan depending on the combined resistance from both the density and viscosity aspects. For example, the lubrication layer is still present between the slab and strong lower mantle in the end-member models with the highest viscosity of the lower mantle (10^{23} Pa·s) and large Clapeyron slopes of C_{660} = -3 or -4 MPa/K (Figures 5n and 5o). However, the slab has already touched the strong lower mantle in other models with relatively low resistances (e.g., Figures 2o, 3o and 5k-m), although all the models terminate at a similar time of about 30 Myr. It indicates that both the high viscosity of the lower mantle and the large Clapeyron slope of C_{660} contribute to the sub-horizontal slab movement along the weak layer beneath D660. In addition, these two factors can compensate each other on the slab flattening at the bottom of the MTZ. For example, the weak layer at 660-710 km can only take effect with the largest C_{660} = -4 MPa/K in the models with an intermediate viscosity of lower mantle (Figures 2o, 3o); however, it contributes to slab flattening with lower C_{660} but a higher viscosity of lower mantle (Figures 5k-m). In addition, the weakest lower mantle prevents any effect of the weak layer on increasing slab flattening, even with the largest C_{660} (Figure 3).

4.2. Comparisons with previous models and geological implications

Although a thin weak layer between the upper and lower mantle has been suggested previously based on mineral physics and geoid modeling (*Panasyuk and Hager, 1998; Mitrovica and Forte, 2004; Karato, 2008*), few studies have been conducted to test its effects on subduction dynamics. *Mao and Zhong* (2018) formulated a 3-D global model of mantle convection with prescribed plate and trench motions, and suggested that the weak layer beneath D660 plays a key role for slab stagnation in the MTZ, especially the large horizontal extent of stagnant slabs in the western Pacific. Further on, *Mao and Zhong* (2019) argued that an additional viscosity increase at 1000 km depth may have a similar effect as the thin weak layer beneath D660. However, the current systematic studies with more generic, pure dynamic models indicate that the effect of the weak layer may not be so crucial. It cannot change the general slab mode selection in the MTZ, i.e. penetration versus stagnation. Especially in the models with more realistic viscosities of the lower mantle (Figures

2-3), the weak layer can only result in a bit longer slab stagnation with a very large Clapeyron slope of C_{660} = -4 MPa/K. In all the other cases, the effect of the weak layer, no matter locating above or beneath D660, is negligible on the subducting slab morphology (Figures 2-3). The detailed comparisons among models in *Mao and Zhong* (2018) also indicate that the weak layer does not change the slab mode from penetration to stagnation (Figure 2 and Supplementary Figure 6 in *Mao and* Zhong, 2018), but does affect the length of stagnant slab, especially in the northern Honshu subduction zone. In this sense, the current 2-D generic model is not conflicting with the previous 3-D global model, but instead suggests a minor role of the thin weak layer at around D660 on the subducting slab dynamics.

5. Conclusions

The discontinuity (D660) at the bottom of the MTZ can strongly affect the subduction dynamics by several factors, i.e. the negative Clapeyron slope ($C_{660} < 0$), the viscosity jump and the plausible presence of a thin weak layer. Their effects are systematically investigated in this study by a series of 2-D generic, pure dynamic models. The main conclusions include the following:

(1) The high viscosity of the lower mantle and the negative Clapeyron slope of phase transition (C_{660}) can both contribute to slab stagnation at the bottom of the MTZ. The effects of these two factors are complementary.

(2) A weak layer above D660, at 610-660 km depth, has negligible effect on the slab morphology in the MTZ.

(3) A weak layer at 660-710 km depth does not modify the slab mode selection (penetration versus stagnation) in the MTZ. However, it contributes to longer slab flattening at the bottom of the MTZ, when strong resistance of the lower mantle is acting on the sinking slab, which may be induced by either a high viscosity jump or a large Clapeyron slope.

(4) The role of the weak layer on slab flattening in the MTZ is strongly dependent on the lubrication effect that promotes the sub-horizontal slab movement along the weak layer at 660-710 km depth.

(5) Previous models without such a weak layer at around D660 are still generally valid, since the weak layer only plays a minor role in the subducting slab dynamics.

Acknowledgement

This work was supported by the Strategic Priority Research Program (B) of CAS (XDB18000000) and the NSFC project (41688103). Numerical simulations were run with the clusters of National Supercomputer Center in Guangzhou (Tianhe-II). *S. Zhong* is acknowledged for the helpful discussion. The figures of numerical models are produced by Matlab and further compiled by Adobe Illustrator. All related data will be provided in the public repository of Zenodo (https://doi.org/10.5281/zenodo.xxxxxxx).

References

Agrusta, R., Goes, S., & van Hunen, J. (2017). Subducting-slab transition zone interaction: stagnation, penetration and mode switches. Earth and Planetary Science Letters, 464, 10-23.

Billen, M. I. (2010). Slab dynamics in the transition zone. Physics of Earth and Planetary Interior, 183, 296-308.

Čížková, H., van Hunen, J., van der Berg, A., & Vlaar, N.J. (2002). The influence of rheological weakening and yield stress on the interaction of slabs with the 670 km discontinuity. Earth and Planetary Science Letters, 199, 447-457.

Corrieu, V., Thoraval, C., & Ricard, Y. (1995). Mantle dynamics and geoid Green functions. Geophysical Journal International, 120, 516-523.

Crameri, F., Schmeling, H., Golabek, G. J., Duretz, T., Orendt, R., Buiter, S., et al. (2012). A comparison of numerical surface topography calculations in geodynamic modelling: An evaluation of the “sticky air” method. Geophysical Journal International, 189(1), 38-54.

Forte, A.M., & Peltier, W.R. (1987). Plate tectonics and aspherical Earth structure: the importance of poloidal-toroidal coupling. Journal of Geophysical Research, 92, 3645-3679.

Forte, A.M., & Peltier, W.R. (1991). Viscous flow models of global geophysical observables. Part 1: Forward problems. Journal of Geophysical Research, 96, 20131-20159.

Forte, A.M., & Mitrovica, J.X. (1996). New inferences of mantle viscosity from joint inversion of long-wavelength mantle convection and post–glacial rebound data. Geophysical Research letters, 23, 1147-1150.

Forte, A.M., Quéré, S., Moucha, R., Simmons, N.A., Grand, S.P., Mitrovica, J.X., & Rowley, D.B. (2010). Joint seismic-geodynamic-mineral physical modelling of African geodynamics: a reconciliation of deep-mantle convection with surface geophysical constraints. Earth and Planetary Science Letters, 295, 329-341.

Gerya, T. V. (2010). Introduction to numerical geodynamic modelling. Cambridge, UK: Cambridge University Press.
Goes, S., Agrusta, R., van Hunen, J., & Garel, F. (2017). Subduction-transition zone interaction: a review. Geosphere, 13 (3), 644-664.
Gurnis, M., & Hager, B.H. (1988). Controls of the structure of subducted slabs. Nature, 335, 317-321.
Hager, B.H., Clayton, R.W., Richards, M.A., Comer, R.P., & Dziewonski, A.M. (1985). Lower mantle heterogeneity, dynamic topography and the geoid. Nature, 313, 541-545.
Karato, S.-I. (2008). Deformation of earth materials: An introduction to the rheology of solid earth. New York: Cambridge University Press.
King, S., & Masters, G. (1992). An inversion for the radial viscosity structure using seismic tomography. Geophysical Research letters, 19, 1551-1554.
Lambeck, K., Johnston, P., Smither, C., & Nakada, M. (1996). Glacial rebound of the British Isles. III. Constraints on mantle viscosity. Geophysical Journal International, 125, 340-354.
Li, Z.-H., Gerya, T., & Connolly, J. A. D. (2019). Variability of subducting slab morphologies in the mantle transition zone: Insight from petrological-thermomechanical modeling. Earth-Science Reviews, 196, 102874.
Liu, H., & Leng, W. (2020). Plume-Tree Structure Induced by Low-Viscosity Layers in the Upper Mantle. Geophysical Research Letters, 47, e2019GL086508.
Mao, W., & Zhong, S. (2018). Slab stagnation due to a reduced viscosity layer beneath the mantle transition zone. Nature Geoscience, 11(11), 876-881.
Mao, W., & Zhong, S. (2019). Controls on global mantle convective structures and their comparison with seismic models. Journal of Geophysical Research: Solid Earth, 124, 9345-9372.
Mitrovica, J.X., & Forte, A.M. (2004). A new inference of mantle viscosity based upon joint inversion of convection and glacial isostatic adjustment data. Earth and Planetary Science Letters, 225, 177-189.
Panasyuk, S. V., Hager, B. H. (1998). A model of transformational superplasticity in the upper mantle. Geophysical Journal International, 133, 741-755.
Ricard, Y., & Bai, W. (1991). Inferring viscosity and the 3-D density structure of the mantle from geoid, topography and plate velocities. Geophysical Journal International, 105, 561-572.
Ricard, Y., Richards, M., Lithgow-Bertelloni, C., & Le Stunff, Y. (1993). A geodynamic model of mantle density heterogeneity. Journal of Geophysical Research, 98, 21895-21909.
Schmeling, H., Babeyko, A. Y., Enns, A., Faccenna, C., Funiciello, F., Gerya, T., et al. (2008). A benchmark comparison of spontaneous subduction models - Towards a free surface. Physics of the Earth and Planetary Interiors, 171(1-4), 198-223.
Steinberger, B., & Calderwood, A.R. (2006). Models of large-scale viscous flow in the Earth's mantle with constraints from mineral physics and surface observations. Geophysical Journal International, 167, 1461-1481.
Sun, W. D., Hawkesworth, C. J., Yao, C., Zhang, C. C., Huang, R. F., Liu, X., et al. (2018). Carbonated mantle domains at the base of the Earth's transition zone. Chemical Geology, 478, 69-75.

Tschauner, O., Huang, S., Greenberg, E., Prakapenka, V. B., Ma, C., Rossman, G. R., et al. (2018). Ice-VII inclusions in diamonds: Evidence for aqueous fluid in Earth's deep mantle. Science, 359(6380), 1136-1139.

Turcotte, D. L., & Schubert, G. (2002). Geodynamics. Cambridge, UK: Cambridge University Press.

Yang, T., Moresi, L., Zhao, D., Sandiford, D., & Whittaker, J. (2018). Cenozoic lithospheric deformation in Northeast Asia and the rapidly-aging Pacific Plate. Earth and Planetary Science Letters, 492, 1-11.

Zhu, T. (2016). Lithospheric stress and upper mantle dynamics in mainland China due to mantle flow based on combination of global- and regional-scale seismic tomography. Journal of Asian Earth Sciences, 132, 103-117.

References from the supporting information

Bina, C. R., & Helffrich, G. (1994). Phase transition Clapeyron slopes and transition zone seismic discontinuity topography. Journal of Geophysical Research, 99(B8), 15,853-15,860.

Bittner, D., & Schmeling, H. (1995). Numerical modeling of melting processes and induced diapirism in the lower crust. Geophysical Journal International, 123, 59-70.

Clauser, C., & Huenges, E. (1995). Thermal conductivity of rocks and minerals. Rock physics & phase relations, 105-126.

Connolly, J. A. D. (2005). Computation of phase equilibria by linear programming: A tool for geodynamic modeling and its application to subduction zone decarbonation. Earth and Planetary Science Letters, 236(1-2), 524-541.

Dziewonski, A. M., & Anderson, D. L. (1981). Preliminary reference Earth model. Physics of the Earth and Planetary Interiors, 25(4), 297-356.

Gorczyk, W., Willner, A. P., Gerya, T. V., Connolly, J. A., & Burg, J. P. (2007). Physical controls of magmatic productivity at Pacific-type convergent margins: Numerical modelling. Physics of the Earth and Planetary Interiors, 163(1-4), 209-232.

Kameyama, M., Yuen, D. A., & Karato, S.-I. (1999). Thermal-mechanical effects of low-temperature plasticity (the peierls mechanism) on the deformation of viscoelastic shear zone, Earth Planet. Science Letters, 1-2, 159-172.

Karato, S., Riedel, M., & Yuen, D. A. (2001). Rheological structure and deformation of subducted slabs in the mantle transition zone: Implications for mantle circulation and deep earthquakes. Physics of the Earth and Planetary Interiors, 127, 83-108.

Karato, S., & Wu, P. (1993). Rheology of the upper mantle: A synthesis. Science, 260(5109), 771-778.

Katz, R. F., Spiegelman, M., & Langmuir, C. H. (2003). A new parameterisation of hydrous mantle melting. Geochemistry, Geophysics, Geosystems, 4(9), 1073.

Kirby, S. H., & Kronenberg, A. K. (1987). Rheology of the lithosphere: selected topics. Reviews of Geophysics, 25, 1219-1244.

Li, Z.-H., Liu, M., & Gerya, T. (2016). Lithosphere delamination in continental collisional orogens: A systematic numerical study. Journal of Geophysical Research: Solid Earth, 121, 5186-5211.

Ranalli, G. (1995). Rheology of the earth, deformation and flow process in geophysics and geodynamics (2nd ed.). London, UK: Chapman & Hall.

Rubie, D. C., & Ross, C. R. (1994). Kinetics of the olivine-spinel transformation in subducting lithosphere: Experimental constraints, and implications for deep slab processes. Physics of the Earth and Planetary Interiors, 86, 223-241.
Schmidt, M. W., & Poli, S. (1998). Experimentally based water budgets for dehydrating slabs and consequences for arc magma generation. Earth and Planetary Science Letters, 163(1-4), 361-379.

AGU PUBLICATIONS

Geophysical Research Letters

Supporting Information for

Effect of a thin weak layer at around the 660-km discontinuity on subducting slab morphology in the mantle transition zone

Zhong-Hai Li [1], Ling Chen [2,3]

[1] Key Laboratory of Computational Geodynamics, College of Earth and Planetary Sciences, University of Chinese Academy of Sciences, Beijing, China.

[2] State Key Laboratory of Lithospheric Evolution, Institute of Geology and Geophysics, Chinese Academy of Sciences, Beijing, China

[3] CAS Center for Excellence in Tibetan Plateau Earth Sciences, Beijing, China

Contents of this file

Introduction

This supporting Information includes:

Text S1 summarizes the numerical methods.

Figure S1 shows the previous inferences of depth-dependent effective mantle viscosity.

Table S1 shows the viscous flow laws used in the numerical experiments.

Table S2 shows the material properties used in the numerical experiments.

Text S1.

1. Governing equations

The numerical models are conducted with the code I2VIS, which combines the finite difference and marker-in-cell methods (*Gerya, 2010*). Three sets of conservation equations (mass, momentum and energy) with the constitutive relationships are solved in the two-dimensional regime.

(1) Stokes equation:

$$\frac{\partial \sigma'_{ij}}{\partial x_j} = \frac{\partial P}{\partial x_i} - g_i \rho(C, M, P, T) \qquad (i, j = 1, 2)$$

Where σ' is the deviatoric stress tensor; x is the spatial coordinate; g is the gravitational acceleration; the density ρ depends on composition (C), melt fraction (M), dynamic pressure (P) and temperature (T). For a specific rock type:

$$\rho = \rho_{\mathrm{solid}} - M(\rho_{\mathrm{solid}} - \rho_{\mathrm{molten}})$$
$$\rho_{\mathrm{solid\,|\,molten}} = \rho_0 \left[1 - \alpha(T - T_0)\right]\left[1 + \beta(P - P_0)\right]$$

Where ρ_0 is the density under the reference condition with P_0 = 0.1 MPa and T_0 = 298 K. α and β are the thermal expansion coefficient and the compressibility coefficient, respectively. Rock density is further corrected for phase transitions.

The constitutive relationship is shown below:

$$\sigma'_{ij} = 2\eta_{\mathrm{eff}} \dot{\varepsilon}_{ij}$$
$$\dot{\varepsilon}_{ij} = \frac{1}{2}\left(\frac{\partial v_i}{\partial x_j} + \frac{\partial v_j}{\partial x_i}\right)$$

Where $\dot{\varepsilon}$ and v are the deviatoric strain rate tensor and velocity vector, respectively. η_{eff} is the effective viscosity.

(2) Incompressible continuity equation:

$$\frac{\partial v_i}{\partial x_i} = 0$$

(3) Energy equation:

$$\rho C_p \left(\frac{DT}{Dt}\right) = -\frac{\partial q_i}{\partial x_i} + H$$
$$q_i = -k(C, P, T)\frac{\partial T}{\partial x_i}$$

Where DT/Dt is the substantive time derivative of temperature; C_p is the effective isobaric heat capacity; q is the thermal heat flux; H represents the heat generations, including radioactive heat production (H_r), adiabatic heating (H_a) and shear heating (H_S). k is the thermal conductivity, dependent on composition (C), pressure (P) and temperature (T).

2. Visco-Plastic-Peierls rheology

(1) Viscous flow law of crustal rocks:

The viscosities of both the continental and oceanic crustal rocks are calculated according to the flow laws of *Ranalli* (1995):

$$\eta_{\text{ductile}} = \frac{1}{2}(A_R)^{-\frac{1}{n}}(\dot{\varepsilon}_{II})^{\frac{1-n}{n}}\exp(\frac{E+PV}{nRT})$$

Where A_R (pre-exponential factor), n (creep exponent), E (activation energy) and V (activation volume) are experimentally determined flow law parameters (A* and B* in Table S1); $\dot{\varepsilon}_{II} = (0.5\dot{\varepsilon}_{ij}\dot{\varepsilon}_{ij})^{1/2}$ is the second invariant of strain rate tensor; R is the gas constant.

(2) Viscous flow law of mantle rocks:

The rheology of mantle rocks is defined according to *Karato and Wu* (*1993*), integrating both diffusion and dislocation creep:

$$\eta_{\text{diffusion | dislocation}} = \frac{1}{2}(A_K)^{-\frac{1}{n}}u\left(\frac{d}{b}\right)^{\frac{m}{n}}(\dot{\varepsilon}_{II})^{\frac{1-n}{n}}\exp(\frac{E+PV}{nRT})$$

$$\frac{1}{\eta_{\text{ductile}}} = \frac{1}{\eta_{\text{diffusion}}} + \frac{1}{\eta_{\text{dislocation}}}$$

Where u is the shear modulus (u = 80GPa); b is the length of Burgers vector (b = 0.5nm); d is grain size (d = 1mm); m is the grain size exponent. Similarly, A_K (pre-exponential factor), n (creep exponent), E (activation energy) and V (activation volume) are flow law parameters determined from the laboratory experiments (C*, D*, E* and F* in Table S1).

(3) Plastic deformation:

The extended Drucker-Prager yield criterion is applied:

$$\eta_{\text{plastic}} = \frac{\sigma_{\text{yield}}}{2\dot{\varepsilon}_{II}}$$

$$\sigma_{\text{yield}} = C_0 + P\sin(\varphi_{\text{eff}})$$

Where σ_{yield} is the yield stress; C_0 is the residual rock strength at P=0; P is the dynamic pressure; φ_{eff} is the effective internal frictional angle, which includes the possible pore fluid/melt effects that control the brittle strength of fluid/melt containing porous or fractured media (*Li et al., 2016*).

(4) Peierls deformation:

The Peierls mechanism is also included for the deformation by low-temperature and high-stress plasticity (e.g., *Kameyama et al., 1999; Karato et al., 2001*).

$$\eta_{\text{peierls}} = \frac{1}{2A_{\text{peierls}}\sigma_{\text{II}}} \exp\left(\frac{E+PV}{RT}\left(1-\left(\frac{\sigma_{\text{II}}}{\sigma_{\text{peierls}}}\right)^{p}\right)^{q}\right)$$

Where A_{peierls}, p, and q are experimentally derived material constants. σ_{II} is the second invariant of stress tensor; σ_{peierls} is a stress value that limits the strength of the material.

(5) Integrated rheology:

The effective viscosity is defined as the minimum value among the ductile viscosity (η_{ductile}), the plastic equivalent (η_{plastic}), and the Peierls viscosity (η_{peierls}) (*Ranalli, 1995*), i.e. $\eta_{\text{eff}} = \min(\eta_{\text{ductile}}, \eta_{\text{plastic}}, \eta_{\text{peierls}})$. The final viscosity is further controlled by the prescribed cut-off values of [10^{18}, 10^{25}] Pa·s.

3. Dehydration and water migration

The numerical model includes both the connate water and mineral water. The connate water, present in sediment and oceanic upper crustal basalt, makes up to 1.0wt% at the surface and decreases to zero at 25 km:

$$X_{\text{H}_2\text{O(wt.\%)}} = (1-\frac{\Delta z}{25})X_{\text{H}_2\text{O}(p_0)}$$

Where Δz is the depth below the surface (0-25 km); $X_{\text{H}_2\text{O}(p_0)}$ is the connate water content at the surface (1.0wt%). For the oceanic lower crust, continental crust and mantle, the connate water content is assumed to be negligible.

The mineral-bound water capacity is computed with Perple_X (*Connolly, 2005*) as a function of pressure and temperature for four typical rock types in the subduction models, i.e. sediment, basalt (oceanic upper crust), gabbro (oceanic lower crust) and hydrated mantle (*Li et al., 2019*). The representative model rock compositions, mineral phases and thermodynamic data sources are shown in *Li et al.* (2019).

The propagation of water is modeled in the form of markers: dehydration reactions lead to a release of water, which is stored in a newly generated water marker. The water markers move through the rocks with the following velocity:

$$v_{i(\text{water})} = v_i - A\left(\frac{\partial P}{\partial x_i} - g_i\rho_{\text{fluid}}\right)$$

$$A = \frac{v_{\text{percolation}}}{g_2(\rho_{\text{mantle}} - \rho_{\text{fluid}})}$$

Where $v_{i(\text{water})}$ is the fluid velocity; v_i is the local velocity of solid rock; A is a water percolation constant with a presumed standard value of $v_{\text{percolation}}$ = 10 cm/yr (e.g., *Gorczyk et al., 2007*); g_2 = 9.81 m/s^2 is the vertical gravitational acceleration component; ρ_{mantle} and ρ_{fluid} are the rock and fluid densities, respectively. When a moving water marker meets a lithology capable of absorbing water by hydration or partial melting reactions at given P–T conditions and rock composition, the water will be consumed.

4. Partial melting

Partial melting of both the crustal and mantle rocks is implemented. For the mantle rocks, the water-content-dependent parameterization of *Katz et al.* (2003) is applied, which is however limited to the depths of <300 km, because this model is inaccurate when extending to larger pressure. On the other hand, for a given crustal rock type, the volumetric degree of melting is assumed to be a linear function of temperature:

$$M = 0,\ \text{when:} T \le T_{\text{solidus}}$$
$$M = \frac{(T - T_{\text{solidus}})}{(T_{\text{liquidus}} - T_{\text{solidus}})},\ \text{when:} T_{\text{solidus}} < T < T_{\text{liquidus}}$$
$$M = 1,\ \text{when:} T \ge T_{\text{liquidus}}$$

Where T_{solidus} and T_{liquidus} are the solidus and liquidus temperatures, respectively, which are specified for each rock type and dependent on the pressure (Table S2) (*Schmidt and Poli, 1998; Katz et al., 2003*).

5. Phase transitions

The phase transitions at 410 km and 660 km discontinuities are implemented in the numerical models (e.g., *Bina and Helffrich, 1994*), which modify the mantle density structure in addition to the gradual pressure and temperature dependence. The Clapeyron slope of phase transition at 410 km has a constant value of 3 MPa/K throughout this study, whereas the one at 660 km is varied with systematically testing its effects on subducting slab dynamics. The resulting density structure of the mantle is consistent with the Preliminary Reference Earth Model (PREM) (*Dziewonski and Anderson, 1981*). Two additional phase transitions are also implemented, i.e. the oceanic crustal eclogitization (*Ito and Kennedy, 2013*) and the metastable olivine in the MTZ (*Rubie and Ross, 1994*), with detailed algorithms summarized in *Li et al.* (2019).

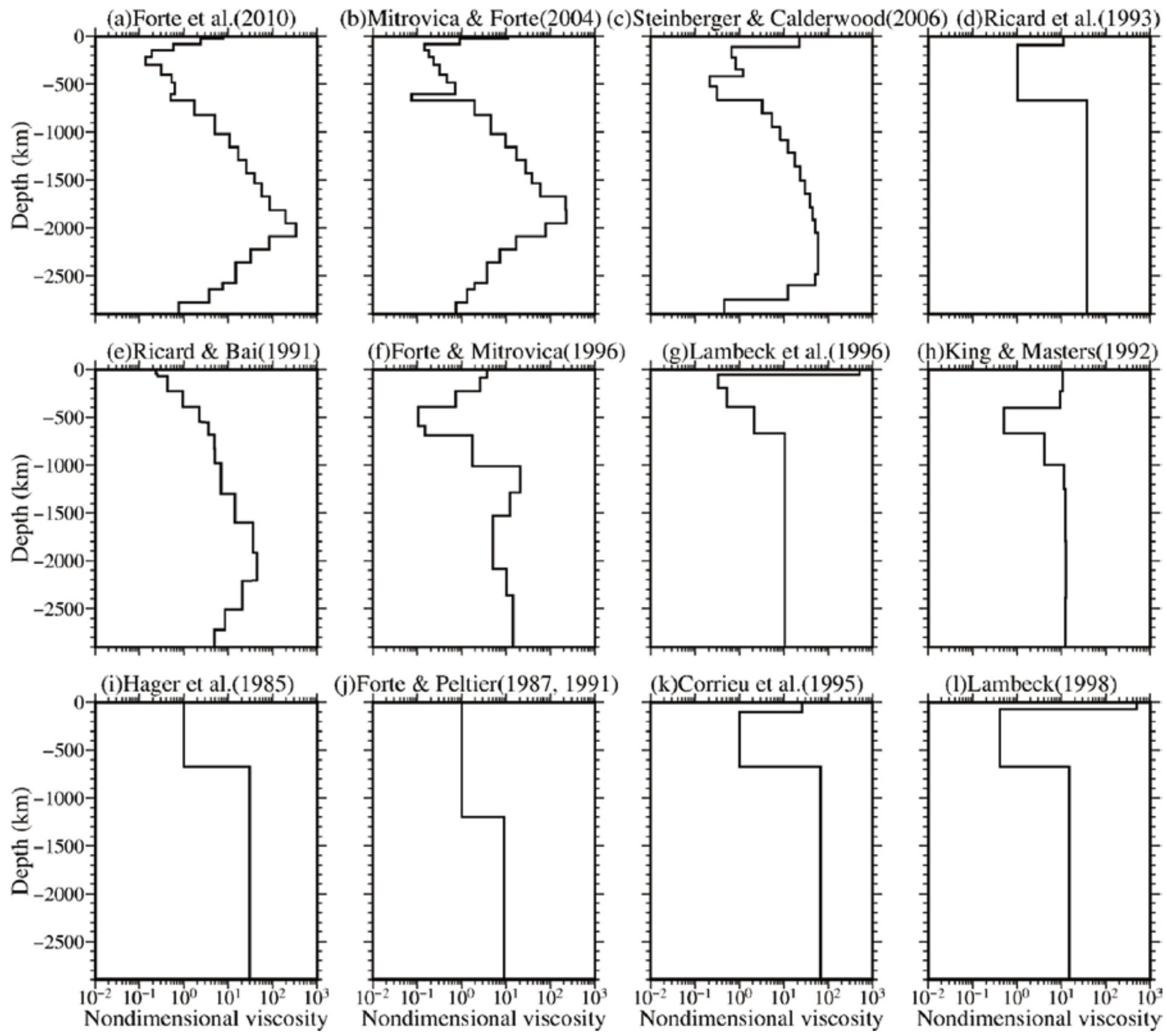

Figure S1. Previous inferences of depth-dependent effective mantle viscosity, as compiled by *Zhu* (2016). (a) and (b) are inferred from joint inversions of global convection-related observables and glacial isostatic adjustment (GIA) data (*Mitrovica and Forte, 2004; Forte et al., 2010*). (c) is inferred from mineral physics and surface observations (*Steinberger and Calderwood, 2006*). (d), (e) and (h)–(k) are derived on the basis of global long wavelength geoid anomalies (*Hager et al., 1985; Forte and Peltier, 1987, 1991; Ricard and Bai, 1991; King and Masters, 1992; Ricard et al., 1993; Corrieu et al., 1995*). (f), (g) and (l) are inferred mainly on the basis of GIA data (*Forte and Mitrovica, 1996; Lambeck et al., 1996, 1998*).

Table S1. Viscous flow laws used in the numerical experiments [a].

Symbol	Flow Law	***E*** (kJ·mol^{-1})	***V*** (J·MPa^{-1}·mol^{-1})	***n***	$\boldsymbol{A_R}$ (MPa^{-n}·s^{-1})	***m***	$\boldsymbol{A_K}$ (s^{-1})
A*	Wet quartzite	154	8	2.3	3.2×10^{-4}	-	-
B*	Plagioclase An_{75}	238	8	3.2	3.3×10^{-4}	-	-
C*	Dislocation creep of dry olivine	540	13	3.5	-	0.0	3.5×10^{22}
D*	Diffusion creep of dry olivine	300	4	1.0	-	2.5	8.7×10^{15}
E*	Dislocation creep of wet olivine	430	10	3.0	-	0.0	2.0×10^{18}
F*	Diffusion creep of wet olivine	240	4	1.0	-	2.5	5.3×10^{15}

[a] Viscous parameters of crustal rocks (A* and B*) are from *Kirby and Kronenberg* [1987] and *Ranalli* [1995]. Viscous parameters of mantle rocks (C*, D*, E*, F*) are from *Karato and Wu* [1993].

Table S2. Material properties used in the numerical experiments [a)].

Material (state)	ρ_0 (kg·m^{-3})	C_p (J·kg^{-1}·K^{-1})	k [b)] (W·m^{-1}·K^{-1})	$T_{solidus}$ [c)] (K)	$T_{liquidus}$ [d)] (K)	Q_L (kJ·kg^{-1})	H_r (μW·m^{-3})	**Viscous** [e)] Flow law	**Plastic** [f)] C_0 (MPa)	**Plastic** [f)] sin(φ_{eff})
Sediment (solid)	2600	1000	K_1	T_{S1}	T_{L1}	300	2.0	A*	10~1	0.1~0.05
Sediment (partial molten)	2400	1000	K_1	T_{S1}	T_{L1}	300	2.0	A*	10~1	0
Continental upper crust (solid)	2800	1000	K_1	T_{S1}	T_{L1}	300	1.0	A*	10~1	0.1~0.05
Continental upper crust (partial	2400	1000	K_1	T_{S1}	T_{L1}	300	1.0	A*	10~1	0
Continental lower crust (solid)	3000	1000	K_1	T_{S3}	T_{L3}	380	1.0	B*	10~1	0.1~0.05
Continental lower crust (partial	2400	1000	K_1	T_{S3}	T_{L3}	380	1.0	B*	10~1	0
Oceanic upper crust (solid)	3000	1000	K_2	T_{S2}	T_{L2}	380	0.25	A*	10~1	0.1~0.05
Oceanic upper crust (partial molten)	2900	1000	K_2	T_{S2}	T_{L2}	380	0.25	A*	10~1	0
Oceanic lower crust (solid)	3000	1000	K_2	T_{S3}	T_{L3}	380	0.25	B*	10~1	0.3~0.15
Oceanic lower crust (partial molten)	2900	1000	K_2	T_{S3}	T_{L3}	380	0.25	B*	10~1	0
Mantle (solid)	3300	1000	K_3	T_{S4}	T_{L4}	400	0.022	C*+D*	10~1	0.3~0.15
Mantle (hydrated)	3300	1000	K_3	T_{S4}	T_{L4}	400	0.022	E*+F*	10~1	0.1~0.05
Mantle (partial molten)	2900	1000	K_3	T_{S4}	T_{L4}	400	0.022	E*+F*	10~1	0
References [g)]	1,2	1,2	3	6,7	6,7	1,2	1	4,5	-	-

[a)] The thermal expansion coefficient $\alpha=2\times10^{-5}$ K^{-1} and the compressibility coefficient $\beta=0.75\times10^{-5}$ MPa^{-1} are used for all rock types.

[b)] $K_1=[0.64+807/(T_K+77)]\cdot\exp(0.00004P_{MPa})$; $K_2=[1.18+474/(T_K+77)]\cdot\exp(0.00004P_{MPa})$; $K_3=[0.73+1293/(T_K+77)]\cdot\exp(0.00004P_{MPa})$.

[c)] T_{S1}={889+17900/(P+54)+20200/(P+54)^2 at P<1200 MPa} or {831+0.06P at P>1200 MPa}; T_{S2}={973-70400/(P+354)+778×10^5/(P+354)^2 at P<1600 MPa} or {935+0.0035P+0.0000062P^2 at P>1600 MPa}; T_{S3}=1327+0.0906P; T_{S4}=KATZ2003.

[d)] T_{L1}=1262+0.09P; T_{L2}=1423+0.105P; T_{L3}=1423+0.105P; T_{L4}=KATZ2003.

[e)] Parameters of viscous flow laws are shown in Table S1.

[f)] Strain weakening effect is included in plastic rheology, in which both cohesion C_0 and effective friction angle sin(φ_{eff}) decrease with larger strain rate.

[g)] References: 1-*Turcotte and Schubert* [2002]; 2-*Bittner and Schmeling* [1995]; 3-*Clauser and Huenges* [1995]; 4-*Ranalli* [1995]; 5-*Karato and Wu* [1993]; 6-*Schmidt and Poli* [1998]; 7-*Katz et al.* [2003].